Journal of Molecular Structure 1352 (2026) 144508

Contents lists available at ScienceDirect

Journal of Molecular Structure

journal homepage: www.elsevier.com/locate/molstr

Synthesis, structural characterization, biological and *in silico* evaluation of halogenated Schiff bases as potential multifunctional agents

Tsholofelo S. Nthehang [a], Ibrahim Waziri [a,*], Tunde L. Yusuf [b], Samson O. Oselusi [c], Alfred J. Muller [a]

[a] Research Centre for Synthesis and Catalysis, Department of Chemical Sciences, University of Johannesburg, P.O. BOX 524, Auckland Park 2006, Johannesburg, South Africa
[b] Department of Chemistry, Faculty of Natural Science and Agricultural Science, University of Pretoria, Private Bag X20, Hatfield 0028 Pretoria, South Africa
[c] Department of Biotechnology, University of the Western Cape, Private Bag X17, Bellville, Cape Town 7535, South Africa

ARTICLE INFO

Key words:
Halogenated schiff bases
Cytotoxicity
Antioxidant
Antibacterial
Molecular docking and dynamics

ABSTRACT

The rising global burden of antimicrobial resistance, oxidative stress–related disorders, and cancer has intensified the search for multifunctional molecules with broad therapeutic potential. In this study, three halogen-substituted Schiff bases (SB1–SB3) were synthesized *via* the condensation of 2-tert-butylaniline with 3,5-dichloro-, 3,5-dibromo-, and 3,5-diiodosalicylaldehyde, respectively. The compounds were characterized using FTIR, UV–Vis, ^{1}H and ^{13}C NMR, mass spectrometry, CHN elemental analysis, and single-crystal X-ray diffraction to confirm their structural integrity and purity. Cytotoxicity screening against the ME180 cervical cancer cell line revealed potent activity, with SB2 (bromo-substituted) showing the lowest IC_{50} (0.60 μM), followed by SB1 (chloro, 0.72 μM) and SB3 (iodo, 1.03 μM). Antioxidant evaluation using the DPPH radical scavenging assay indicated moderate, dose-dependent activity, with SB1 exhibiting the highest scavenging rate (37.6–38.8 %). Antibacterial assays against *Staphylococcus. aureus, Staphylococcus. pyogenes, Escherichia coli*, and *Klebsiella. pneumoniae* demonstrated SB1's superior inhibitory effect and lowest MIC values, particularly against *S. pyogenes* and *K. pneumoniae* .Computational analyses, including molecular docking, molecular dynamics simulations (MDS), and ADMET profiling, supported the experimental findings. The compounds exhibited favourable binding affinities, especially through Zn^{2+} coordination and interactions with Glu402 and His411. MDS confirmed the stability of SB1 and SB3 over 150 ns, while ADMET results highlighted SB1's promising drug-like characteristics.

1. Introduction

The global incidence of cancer continues to rise at an alarming rate, posing a significant challenge to public health worldwide [1,2]. Among the various underlying mechanisms implicated in cancer development and progression, oxidative stress plays a critical role by inducing cellular damage through the generation of reactive oxygen species (ROS) [3–5]. This has led to an intensified search for effective therapeutic agents that possess both anticancer and antioxidant properties. At the same time, antimicrobial resistance (AMR) has emerged as another pressing global health crisis [6,7]. The misuse and overuse of antibiotics in both clinical and agricultural settings have accelerated the evolution of multidrug-resistant bacterial strains, severely undermining the effectiveness of conventional antibiotics [8,9]. This not only compromises the treatment of infectious diseases but also complicates critical medical interventions such as chemotherapy, organ transplantation, and major surgeries, where infection control is essential [10]. The urgent need for new antimicrobial agents that can overcome resistance mechanisms has therefore become a priority in modern drug discovery [11,12].

In recent years, Schiff bases have garnered considerable attention due to their structural versatility, ease of synthesis, and wide range of biological activities [13,14]. Schiff bases derivatives or scaffolds, particularly those incorporating halogen and alkyl substituents, have demonstrated promising potential as dual-function therapeutic agents [15,16]. Halogens such as chlorine, bromine, and iodine are known to enhance biological activity through increased lipophilicity and membrane permeability, while bulky alkyl groups like tertiary butyl can contribute to improved stability and selective interaction with biological targets [17–19].

Although extensive studies have examined Schiff bases with halogen

* Corresponding author.
E-mail address: triumph2236@gmail.com (I. Waziri).

https://doi.org/10.1016/j.molstruc.2025.144508
Received 30 August 2025; Received in revised form 11 October 2025; Accepted 23 October 2025
Available online 23 October 2025

or alkyl substituents, limited attention has been given to systems that incorporate both features within the same molecular scaffold. Such a combination could produce synergistic effects, leading to enhanced anticancer, antioxidant, and antimicrobial efficacy, including the potential to address bacterial resistance [20].

Therefore, exploring Schiff bases containing both halogen and tertiary butyl substituents represents a promising strategy in the ongoing development of multifunctional compounds with enhanced biological efficacy.

2. Experimental

2.1. Materials and instruments

The chemicals and reagents used in this research were procured from Merck Pty Ltd and were utilized without further modifications. Proton and carbon nuclear magnetic resonance (NMR) spectra were acquired using a 500 MHz and 125 MHz NMR spectrometer for proton and carbon, respectively, at room temperature. DMSO-d_6 was used as the solvent, with chemical shifts expressed as $\delta_H = 2.50$ ppm and $\delta_C = 39.50$ ppm. Infrared (IR) spectra of the compound were obtained using a Perkin-Elmer BX spectrometer. The elemental composition (CHN) of the compounds was determined using a VarioElementarIII CHN microanalyzer. The molecular weight was estimated using a high-resolution mass spectrometer (Waters Acquity UPLC Synapt G2 HD).

2.2. Synthesis of the Schiffbase compounds (SB1-SB3)

Schiff base compounds are typically synthesized through a condensation reaction between a carbonyl compound and a primary amine in an alcoholic medium, using either an acid- or base-catalyzed reaction [21]. In this study, we employed substituted salicylaldehyde (dichloro, dibromo, or diiodo derivatives) and 2-tertiarybutyl aniline.

In general, 2-tertiarybutyl aniline (0.27 g, 1.8 mmol, 1 eq) was dissolved in 20 mL of methanol and added to a stirring methanolic solution of 3,5-dichlorosalicylaldehyde (0.34 g, 1.8 mmol, 1 eq), 3,5-dibromosalicylaldehyde (0.50 g, 1.8 mmol, 1 eq), or 3,5-diiodosalicylaldehyde (0.67 g, 1.8 mmol, 1 eq), each dissolved in 20 mL of methanol in separate reaction flasks. Subsequently, three drops of formic acid were added to each solution, resulting in the formation of an instant precipitate. The solutions containing the precipitate were further stirred for four hours at 65 °C. The resulting precipitate was filtered, dried, and, if no precipitate formed, crushed ice was added to the reaction mixture, which led to the formation of a precipitate. The product obtained was then dried and re-crystallized in methanol. The pathway leading to the formation of the compounds is shown in Scheme 1, and a detailed description of the extracted spectroscopic and physicochemical data for each compound is provided below.

2.3. (Z)-2-(((2-(tert-butyl)phenyl)imino)methyl)-4,6-dichlorophenol (SB1)

Yield: (0.45 g, 78.0 %); yellow solid; m.p. 128–130 °C; ^{1}H NMR (500 MHz, DMSO–d_6, δ ppm): 13.85 (s, 1H, -OH), 8.73 (s, 1H, -HC═*N*), 7.78 (d, 1H, $J = 2.0$ Hz, Ar-H), 7.73 (d, 1H, $J = 2.0$ Hz, Ar-H), 7.43 (d, 1H, $J = 7.5$ Hz, Ar-H), 7.34–7.27 (m, 2H, $J = 6.5$ Hz, Ar-H), 7.11 (d, 1H, $J = 7.5$ Hz, Ar-H), 1.37 (s, 9H, t-bu-H); ^{13}C NMR (125 MHz, DMSO-d_6, δ ppm): 162.0 (-*C* = *N*), 154.8 (C—OH, Ar-C), 147.4, 142.2, 132.2, 130.5, 127.4, 127.1, 126.2, 122.5, 121.4, 121.3, 121.1 (Ar-C), 34.8, 30.5 (t-bu-C); IR_{ATR}: ν_{max}/cm^{-1}: $\nu_{(OH)} = 3000$, $\nu_{(C—H(Ar))} = 2850$, $\nu_{(C\,=\,N)} = 1608$, $\nu_{(CH3)} = 1438$, $\nu_{(C—N)} = 1346$, $\nu_{(C—O)} = 1220$, $\nu_{(C—Cl)} = 686$; UV–Visible (DMSO, 10^{-3} M): λ_{max}/nm: 230 (π→π*), 270 (π→π*), 349 (n→π*); CHN Anal. Calculated for $C_{17}H_{17}Cl_2NO$: C, 63.37; H, 5.32; N, 4.35; Found: C, 64.43; H, 5.39; N, 4.68; HRMS-ESI: Calculated for $C_{17}H_{17}Cl_2NO = 322.0765$ $[M + H]^+$; Found = 322.0765

2.4. (Z)-2,4-dibromo-6-(((2-(tert-butyl)phenyl)imino)methyl)phenol (SB2)

Yield: (0.62 g, 84.0 %); orange solid; m.p. 123–126 °C; ^{1}H NMR (500 MHz, DMSO–d_6, δ ppm): 14.05 (s, 1H, -OH), 8.70 (s, 1H, -HC═*N*), 7.93 (d, 2H, $J = 1.5$ Hz, Ar-H), 7.43 (t, 1H, $J = 7.0$ Hz, Ar-H), 7.34–7.27 (m, 2H, $J = 6.5$ Hz, Ar-H), 7.12 (t, 1H, $J = 7.0$ Hz, Ar-H), 1.36 (s, 9H, t-bu-H); ^{13}C NMR (125 MHz, DMSO-d_6, δ ppm): 161.7 (-*C* = *N*), 155.7 (C—OH, Ar-C), 146.7, 141.7, 137.0, 133.8, 126.7, 125.7, 121.0, 120.9, 110.6, 109.4 (Ar-C), 34.3, 30.0 (t-bu-C); IR_{ATR}: ν_{max}/cm^{-1}: $\nu_{(OH)} = 3000$, $\nu_{(C—H(Ar))} = 2900$, $\nu_{(C\,=\,N)} = 1612$, $\nu_{(CH3)} = 1427$, $\nu_{(C—N)} = 1345$, $\nu_{(C—O)} = 1176$, $\nu_{(C\text{-}Br)} = 686$; UV–Visible (DMSO, 10^{-3} M): λ_{max}/nm: 240 (π→π*), 275 (π→π*), 345 (n→π*); CHN Anal. Calculated for $C_{17}H_{17}Br_2NO$: C, 49.66, H, 4.17; N, 3.41 Found: C, 49.64; H, 4.16; N, 3.39; HRMS-ESI: Calculated for $C_{17}H_{17}Br_2NO = 411.9735$ $[M + H]^+$; Found = 411.9731

2.5. (Z)-2-(((2-(tert-butyl)phenyl)imino)methyl)-4,6-diiodophenol (SB3)

Yield: (0.71 g, 78.0 %); orange solid; m.p. 130–132 °C; ^{1}H NMR (500 MHz, DMSO–d_6, δ ppm): 14.15 (s, 1H, -OH), 8.60 (s, 1H, -HC═*N*), 8.15 (d, 1H, $J = 2.0$ Hz, Ar-H), 8.03 (d, 1H, $J = 2.0$ Hz, Ar-H), 7.42 (d, 1H, $J = 1.5$ Hz, Ar-H), 7.41–7.09 (m, 2H, $J = 1.5$ Hz, Ar-H), 7.08 (d, 1H, $J = 1.5$ Hz, Ar-H), 1.36 (s, 9H, t-bu-H); ^{13}C NMR (125 MHz, DMSO-d_6, δ ppm): 162.3 (-*C* = *N*), 159.1 (C—OH, Ar-C), 148.4, 147.3, 142.1, 141.0, 127.4, 127.0, 126.1, 121.6, 121.1, 87.5, 81.4, (Ar-C), 34.8, 30.5 (t-bu-C); IR_{ATR}: ν_{max}/cm^{-1}: $\nu_{(OH)} = 3000$, $\nu_{(C—H(Ar))} = 2862$, $\nu_{(C\,=\,N)} = 1604$, $\nu_{(CH3)} = 1435$, $\nu_{(C—N)} = 1269$, $\nu_{(C—O)} = 1153$, $\nu_{(C\text{-}I)} = 659$; UV–Visible (DMSO, 10^{-3} M): λ_{max}/nm: 238 (π→π*), 279 (π→π*), 348 (n→π*); CHN Anal. Calculated for $C_{17}H_{17}I_2NO$: C, 40.42, H, 3.39; N, 2.77 Found: C, 39.33; H, 3.38; N, 2.78; HRMS-ESI: Calculated for $C_{17}H_{17}I_2NO = 505.9501$ $[M + H]^+$; Found = 505.9489

2.6. Single-crystal X-ray diffraction analysis

Crystallographic data for the compounds were obtained using an APEXII instrument with Mo Ka radiation (λ = 0.71073 Å) at a temperature of 293 K. The collected frames underwent processing for integration purposes using Bruker SAINT [22]. Subsequently, absorption effects were minimized through the application of SADABS [23], and the

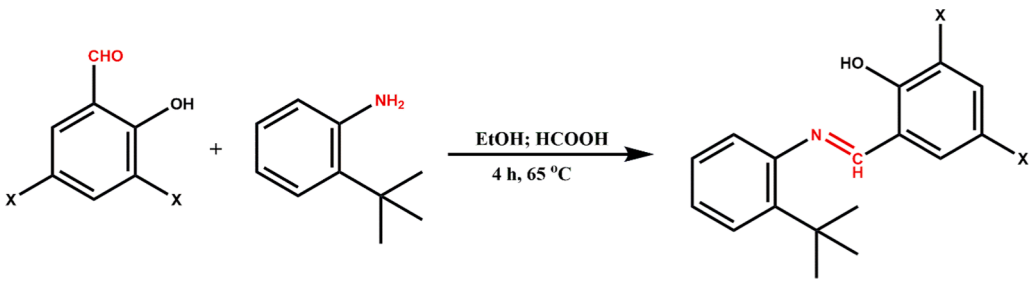

Scheme 1. Pathway for the synthesis of the Schiff bases (SB1: *X* = Cl; SB2: *X* = Br; and SB3: *X* = *I*).

structures were solved with SHELXT [24]. Refinement of the structures was conducted using SHELXL [24]. Crystal structure graphics were generated utilizing Mercury software [25]. Non-hydrogen atoms were initially refined isotropically and later anisotropically through the least squares method. Hydrogen atoms were placed geometrically and refined using a riding approximation [26].

3. Biological study

3.1. Stability study in aqueous buffer

The stability of the compounds was evaluated in an aqueous/DMSO mixture. Each compound was dissolved in a solution of 5 % DMSO–KH_2PO_4 buffer (50 mM, pH 7.5), and their UV–Vis spectra were monitored over time. Spectral acquisitions were recorded in the range of 200–800 nm at 7-day intervals. The stability study spectra are presented in the supplementary information (Figures S6, S12, and S18).

3.2. Cyto-toxicity study

The cytotoxic potential of the synthesized compounds (SB1–SB3) was evaluated using the MTT assay, following a reported protocol [27]. The ME180 cervical cancer cell line was cultured in a T-flask and incubated at 37 °C with 5 % CO_2 until satisfactory confluency was achieved. Once confluent, the culture medium was removed, and the cells were washed, trypsinized, counted, and resuspended to prepare a seeding solution.

From this suspension, 100 μL containing approximately 1×10^4 cells was dispensed into each well of a 96-well plate. The plates were incubated for 24 h to allow cell attachment prior to treatment. Methylglyoxal served as the positive control, while DMSO was used as the negative control. The test compounds (SB1–SB3) were prepared in DMSO at concentrations of 1 μM and 2 μM.

After incubation, the medium in each well was replaced with 100 μL of fresh DMEM. The compounds were added to the respective wells at volumes of 10 μL (for 1 μM) and 20 μL (for 2 μM), and the plates were further incubated for 24 h.

Subsequently, 10 μL of MTT solution (5 mg/mL) was added to each well, followed by a 4 h incubation at 37 °C with 5 % CO_2. The medium was then removed, and 100 μL of DMSO was added to dissolve the formazan crystals, producing a colour change from yellow to dark purple. The plates were incubated for an additional 1 h, and absorbance was measured at 570 nm using a micro-plate reader. The absorbance values were used to calculate percentage cell viability and IC_{50} was determined from triplicate MTT measurements by nonlinear regression to a 4-parameter logistic model (GraphPad Prism vX). Data were normalized to vehicle controls and plotted as % viability *vs*$\log_{10}$[SB1-SB3]. Best-fit IC_{50} (μM) ± 95 % CI and Hill slope are reported. The ME180 cell line was selected because it is a well-established human cervical carcinoma model widely used in cytotoxicity studies. Methylglyoxal, employed as the positive control, was chosen due to its documented anticancer properties, particularly its ability to induce apoptosis and inhibit cancer cell growth through oxidative stress pathways, making it an appropriate benchmark for comparison. In the present study, cytotoxicity was evaluated using only the ME180 cervical cancer cell line. The inclusion of additional cancer cell lines or a non- cancerous/normal cell line for comparative assessment was not feasible due to the unavailability of these cell lines and associated resources during the study period.

3.3. Antioxidant study

The antioxidant activity of the synthesized compounds (SB1–SB3) was evaluated using the DPPH free radical scavenging assay, following a reported procedure [28]. A stock solution of each compound was prepared at 1000 μM in 10 mL of DMSO, from which working solutions of 50 μM (2 mL) and 25 μM (1 mL) were subsequently prepared. A 0.1 mM DPPH solution was freshly prepared in 35 mL of methanol.

For the assay, samples and the positive control were loaded into separate 96-well plates. Each well received 100 μL of the test solution, after which 100 μL of the DPPH solution was added under dark conditions to minimize photo-degradation. The plates were incubated for 30 min at room temperature, and absorbance was recorded at 515 nm using a micro-plate reader. The reduction in absorbance relative to the control indicated the free radical scavenging activity of the test compounds. The radical scavenging activity was estimated using the formula below:

$$\%\text{Radical Scavenging} = \frac{Absorbance of the control - Absorbance of the sample}{Absorbance of the sample} \times 100$$

3.4. Statistical analysis

All antioxidant assays were performed in triplicate, and the data are presented as mean ± standard deviation (SD). Differences among treatment groups were analyzed using one-way analysis of variance (ANOVA) followed by Tukey's post-hoc test for pairwise comparisons. A p-value of < 0.05 was considered statistically significant. Statistical analyses and graph plotting were performed using GraphPad Prism version 10.0 (GraphPad Software, San Diego, *CA*, USA).

3.5. Antibacterial study

The *in vitro* antimicrobial activities of the synthesized compounds (SB1–SB3) were evaluated using the disc diffusion method [29]. Ciprofloxacin was employed as the positive control, while dimethyl sulfoxide (DMSO) served both as the solvent and negative control. The test panel included two Gram-positive bacterial strains (*Staphylococcus aureus* and *Streptococcus pyogenes*) and two Gram-negative strains (*Escherichia coli* and *Klebsiella pneumoniae*). Sterile nutrient agar plates were prepared by inoculating each medium with a standardized microbial suspension and allowing it to solidify in sterile Petri dishes. Sterile filter paper discs impregnated with 20 μM and 40 μM solutions of the test compounds were carefully placed on the agar surface. The plates were incubated at 37 °C for 24 h, after which antimicrobial activity was assessed by measuring the diameter of the zones of inhibition (mm) surrounding each disc. All experiments were performed in triplicate to ensure reproducibility, and results are expressed as mean ± standard deviation (SD).

3.6. Molecular docking study

The crystal structure of matrix metalloproteinase-9 (MMP-9) in complex with a reverse hydroxamate inhibitor (PDB ID: 1GKC) [30] was retrieved from the Protein Data Bank (https://www.rcsb.org/) for computational analysis. MMP-9 was selected as the docking target due to its key role in extracellular matrix degradation, tumor invasion, and metastasis, including its established role in cervical cancer [31]. Additionally, it contributes to bacterial pathogenesis through tissue remodelling and inflammation [32] Structure preparation was performed using the Protein Preparation Wizard in Schrödinger (Schrödinger, LLC, New York, NY, v13.5), which involves three main steps: import and process, review and modify, and refinement. In the first step, hydrogen atoms were added, bond orders were assigned, and missing side chains were completed. The second step reviewed and modified the structure to retain only chain A. In the final step, hydrogen bonds were optimized, and water molecules >3.0 Å from the protein surface were removed. The structure was then subjected to restrained energy minimization using the OPLS4 force field [33] to optimize geometry and resolve steric clashes. The ligand was prepared using Schrödinger's Ligprep module with the OPLS4 force field. An Epik job was run to model metal-binding interactions and includes the original ionization state. Up to 32

stereoisomer were generated per ligand, respecting specified chirality. Docking was performed by first generating a receptor grid based on the co-crystallized ligand. The receptor grid and prepared ligands were used for extra precision (XP) docking. Docking results were evaluated based on Glide docking scores and the molecular interactions between ligands and protein residues.

3.7. Molecular dynamics

To evaluate the dynamic behaviour and stability of the protein-ligand complex under physiological conditions, molecular dynamics simulations (MDS) were performed using Desmond, integrated within Schrödinger Maestro. The complex, comprising atoms, was solvated in a 10 × 10 × 10 Å orthorhombic periodic box using TIP4P water molecules. The system was neutralized by adding 10 Na^+ counter ions. Energy minimization and positional restraints were applied using the OPLS4 force field. Subsequently, a 150-nanosecond MDS was conducted under NPT ensemble conditions at 300 K and 1.01325 atm, with trajectory snapshots recorded every 100 ps. Post-simulation analysis included evaluation of several parameters such as ligand-binding site stability, root mean square deviation (RMSD), root mean square fluctuation (RMSF), and Solvent Accessible Surface Area (SASA) to assess system stability, compactness, structural fluctuations, and protein-ligand interactions throughout the simulation. The experiment was performed twice to ensure consistency and reproducibility of the simulation results, and the average values from the independent runs are presented.

3.8. Physicochemical properties, drug-likeness, and pharmacokinetic profiling

The SMILES (Simplified Molecular Input Line Entry System) representations of the synthesized compounds were uploaded to the SwissADME (http://www.swissadme.ch/) and pkCSM (https://biosig.lab.uq.edu.au/pkcsm/) web tools to evaluate their physicochemical and pharmacokinetic properties. Lipinski's Rule of Five was used to assess the drug-likeness of the compounds, following the approach described by [34]. The pharmacokinetic potential was predicted based on key ADMET (Absorption, Distribution, Metabolism, Excretion, and Toxicity) parameters. These predictions offered insights into the bioavailability, safety, and suitability of the compounds as potential drug candidates.

4. Results and discussion

4.1. Chemistry

The condensation reaction between 2-tert-butylaniline and salicylaldehyde derivatives, namely 3,5-dichlorosalicylaldehyde, 3,5-dibromosalicylaldehyde, and 3,5-diiodosalicylaldehyde, in methanol, using a catalytic amount of formic acid, afforded the Schiff base compounds **SB1–SB3** (Scheme 1). The products were obtained in good yields (74–84 %) and high purity. They were crystalline solids, exhibiting distinct colours ranging from orange to yellow. The compounds showed good solubility in methanol, ethanol, chloroform, acetone, dichloromethane, dimethyl sulfoxide (DMSO), and dimethylformamide (DMF), and were stable under ambient light and air. Their successful formation was confirmed by a suite of spectroscopic techniques, discussed in detail below.

4.2. Nuclear magnetic resonance study

^1H and ^{13}C NMR was used to analyze and validate the formation of the Schiff base compounds (SB1-SB3). The spectra were recorded in DMSO-d_6 are presented in the supplementary information. The NMR data are consistent with formation of the expected salicylidene Schiff base. In ^1H NMR spectra (Figure S1, S7, and S13), a characteristic intramolecular hydrogen-bonded phenolic OH appears as a strongly deshielded singlet at ≈ 13.85, 14.05, and 14.15 ppm in SB1-SB3, respectively, while the azomethine proton (-HC═*N*) resonates up-field relative to the phenolic group as a singlet at 8.70, 8.73, and 8.60 ppm, respectively, both diagnostic of the salicylidine imine motif and conjugation with aromatic ring [35–37]. The aromatic region (≈ 7.09–8.15 ppm) shows the multiplet pattern expected for the two differently substituted rings; substitution by electron-withdrawing Cl, Br, and I on the aldehyde ring produces the observed chemical-shift dispersion and splitting patterns. The signal due tertiary butyl proton appears upfield at strong singlet at 1.37, 1.36, and 1.35 ppm for SB1-SB3, respectively [38]. The ^{13}C NMR spectra (Figure S2, S8, and S14), supports these proton assignments: the signal due $C = N$ carbon atoms were seen downfield at ≈ 162.0, 161.7, and 162.3 ppm on the spectra of SB1-SB3, respectively and phenolic C—O carbon appears at 154.8, 155.7, and 159.1 ppm, consistent with conjugated salicylidine systems [39,40]. Aromatic carbon resonances are distributed between 120–148 ppm, with the ipso carbon bound to bromine and iodine unusually deshielded/shifted (signal at ≈ 109–110 and 81–87 ppm), a pattern typical of aryl C-Br and C-I carbons [41], and other ring carbons (including those of the tertiary butyl) occupying the expected 30–34 ppm region. Taken together (integrations, multiplicities, and the characteristic downfield phenolic and imine signals in ^1H, plus $C = N$ and C—O resonance in ^{13}C), the NMR data strongly support formation and purity of the synthesized Schiff base compounds (SB1-SB3).

4.3. Infrared spectral study

The infrared spectra of the synthesized Schiff base compounds (SB1-SB3) were recorded in solid using ATR method, the spectra are presented in the supplementary information (Figures S3, S9 and S15). These spectra provide an insight into the molecular structure and bonding characteristics of the compounds. In these spectra, the phenolic O—H stretching appeared as a distinct, low-frequency (in region of 3000 cm^{-1}) in all compounds due to intramolecular O–H···N H-bonding and the $C = N$ stretching was observed within the range of 1604–1612 cm^{-1}. Similarly, aromatic C—H stretching appeared at range of 2850–2900 cm^{-1}. The phenolic C—O band appears at the region of 1153–1220 cm^{-1}, in the range expected for neutral Ar-O-H stretching [42,43]. The tertiary butyl (CH_3) stretching vibrations were observed at the range of 1427–1438 cm^{-1}, while C—N band at 1345–1369 cm^{-1} [44]. Aryl-halide fingerprints (C—Cl and C-Br at 686 cm^{-1}; and C-I at 659 cm^{-1}) persist, confirming the substituents are intact. The FTIR spectra of the compound's dovetails with their ^1H NMR (strongly deshielded O—H at 13.85–14.15 ppm from O–H···N and imine CH at the range of 8.60–8.73 ppm).

4.4. UV–Visible spectral study

The UV–Visible spectra of the compounds were recorded using (10^{-3} M) DMSO solution at wavelength range of 200–800 nm, with spectra presented in the supplementary information (Figures S4, S10, and S16). The spectra show three absorption bands each at 230–240 nm and 270–279 nm arise from π→π* transition of the salicyl/aniline rings and 345–349 nm due conjugated $C = N$ system [45,46]. No significant absorption beyond 350 nm is seen, consistent with a neutral, intramolecular H-bonded salicylidine imine. These UV–Vis spectra are fully consistent with the data obtained from FTIR and NMR study results, collectively substantiating formation of the compounds.

4.5. Mass spectral study

To further affirm and validate the formation compounds, mass spectral study was carryout using high resolution mass spectroscopy in positive injection mode. The spectra obtained from the study are shown the supplementary information (Figures S5, S11, and S17) for SB1-SB3, respectively. In the spectrum of SB1 (Figures S5), the molecular ion is observed at *m/z* 322.0765 assigned to $[M + H]^+$, in excellent agreement

with the calculated exact mass 322.0765 for $[M + H]^+$, which is fully consistent with the proposed elemental formula for the compound and validates clean formation of the SB1. In the spectrum of SB2 (Figure S11), the dominant high-mass ion appears at *m/z* 411.9731, assigned to $[M + H]^+$, the calculated exact mass is 411.9735 for $[M + H]^+$(Δ= −0.0004 u). The absolute difference is small negligible (−0.0004 u, ~ 0.0001 %), which strongly corroborate the SB2formulation. Similarly, in the spectrum of SB3 (Figure S17), the molecular ion peak was observed at *m/z* 505.9489, assigned to $[M + H]^+$, the calculated value is 505.9478 for $[M + H]^+$ (Δ= −0.003 u). The absolute difference is −0.0006 %, which strongly supports the formation of the compound.

4.6. Description of crystalstructure

Single-crystal X-ray diffraction unambiguously establishes that all three compounds are salicylaldimine derivatives (Fig. 1) whose molecular conformations are governed by an intramolecular O–H···N interaction that locks the salicyl and imine fragments close to coplanar. SB2 ($C_{17}H_{17}Br_2NO$) and SB3 ($C_{17}H_{17}I_2NO$) are isostructural in $P2_1/c$ with Z′ = 2, whereas SB1 (chlorinated analogue) crystallises in *P*-1 with a markedly higher Z′ = 4. Unit-cell volumes follow the expected halogen trend (SB2: $V \approx 3409$ Å^3; SB3: $V \approx 3629$ Å^3), and the calculated densities increase with atomic number (*ca* 1.60 g cm^{-3} for SB2 and 1.85 g cm^{-3} for SB3), reflecting heavier substituents. In contrast, SB1 ($V \approx 3320$ Å^3, ρ_{calc} ≈ 1.29 g cm^{-3}) packs more loosely despite the larger number of independent molecules in the asymmetric unit. Refinements are chemically sensible throughout: R1($I > 2\sigma$) ≈ 0.048–0.083 with wR2 values commensurate with composition and Z′ (SB1 higher owing to Z′ = 4 and labile-H localisation), all non-H atoms refined anisotropically, and hydrogen treated by constrained riding models.

The contents of the asymmetric unit are a key discriminator. SB2 and SB3 each contain two independent molecules (A/B) that are conformationally similar: both display the classic S(6) intramolecular O–H···N ring, which fixes the phenolic O and imine N in close proximity and enforces planarity across the salicyl–imine junction (representative torsions ~0/180°). By contrast, SB1 contains four independent molecules (A–D). Three (A/B/D) adopt the same phenol–imine tautomer as SB2/SB3, each with a short H···*N* ≈ 1.84–1.89 Å and O···*N* ≈ 2.57–2.59 Å at angles ~142–148°, consistent with a strong intramolecular hydrogen bond. The fourth molecule (C) localises the labile proton at nitrogen, giving an N–H···O contact (N–*H* ≈ 0.86 Å; H···*O* ≈ 1.94 Å; N···*O* ≈ 2.62 Å; ∠ ≈ 136°). This tautomeric heterogeneity rationalises the elevated Z′ in SB1 and subtly perturbs its packing compared with the bromide/iodide congeners.

Molecular metrics are fully consistent with substituted salicylaldimine. In SB2, C–Br distances cluster around 1.88–1.90 Å, while in SB3, C–I spans 2.08–2.10 Å; SB1 shows C–Cl ≈ 1.74–1.76 Å. The C–O (phenolic) bonds are short across the series (typically 1.32–1.35 Å), reflecting partial phenolate character within the intramolecular H-bonded six-membered ring. The imine linkage exhibits the expected contraction, with *C* = *N* ≈ 1.25–1.30 Å and longer adjacent C–N single-bond metrics when applicable. Aromatic C–C values lie in normal ranges. Torsion angles about the imine–aryl junctions are near-planar (representative ≈ 0–3° or 176–180°), highlighting an extended π-conjugation that is reinforced by the S(6) motif.

Both intra- and intermolecular interactions map cleanly onto these metrics. Intramolecularly, the O–H···N S(6) ring is the dominant structure-directing feature in all independent molecules except SB1-C, where N–H···O prevails. Several short O···X (*X* = Cl) approaches occur within SB1 (≈ 2.87–2.89 Å), but with compressed C–Cl···O angles (54°) that are inconsistent with σ-hole donation; they are best regarded as enforced proximities from the ortho-chloro geometry rather than halogen bonds. Intermolecularly, SB2 presents a noteworthy Br···Br approach at ~3.63 Å, slightly below Σr_{vdW}(Br) ≈ 3.70 Å and with near-symmetric approach angles (137°/137°), consistent with a weak Type-I halogen···halogen contact that helps stitch adjacent molecules without generating one-dimensional chains. In SB3, the shortest I···I separation is ~4.50 Å (≫Σr_{vdW}(I) ≈ 3.96 Å), so directional I···I halogen bonding is absent; packing is instead dominated by dispersion and edge-to-face C–H···π contacts. SB1 similarly lacks directional Cl···Cl interactions (shortest ~4.29–4.36 Å, >Σr_{vdW}), and the lattice is organised by a denser web of weak contacts (C–H···π, π···π overlaps) arising from the four independent molecules and the mixed O–H···N/N–H···O

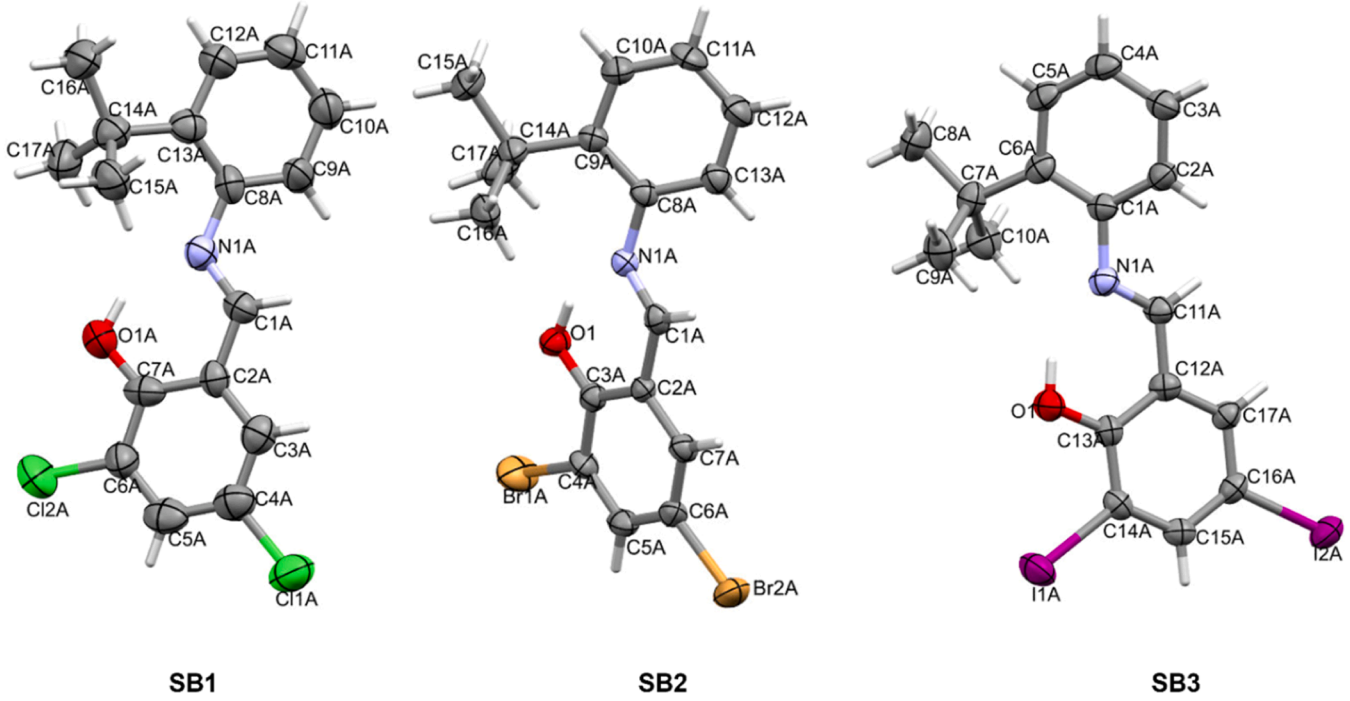

Fig. 1. ORTEP diagrams of the molecular structures of the compounds (SB1-SB3) with 50 % probability ellipsoids for all non-H atoms, while H atoms are represented with arbitrary radius.

tautomerism.

Taken together, these data show a coherent crystal-engineering narrative across the series. The intramolecular S(6) hydrogen bond reliably templates near-planarity and conjugation within each molecule; the nature and geometry of halogens then modulate intermolecular packing only subtly, most clearly through a weak Br···Br contact in SB2 and the absence of analogous I···I or Cl···Cl features in SB3/SB1, respectively. The higher Z′ of SB1, indicates conformational flexibility and a highly interlocked stabilization by multiple hydrogen bonding and halogen-halogen interactions. This dense molecular arrangement enhances lattice stability and could results in the compound's enhanced therapeutic potentials as can be seen in antioxidant and antimicrobial activity results. Because improved solid-state stability and favourable halogen contacts results in better molecular alignment and interaction with biological target. Overall, the crystallographic parameters (space group, Z′ content, bond metrics and non-covalent geometries) are internally consistent and chemically intuitive for halogenated salicylaldimine, and they neatly rationalise the observed packing differences across SB1–SB3. The detailed crystallographic data and refinement parameters are given in Table 1.

Table 1
Crystal data and structure refinement.

Identification code	SB1	SB2	SB3
Empirical formula	$C_{68}H_{69}Cl_8N_4O_4$	$C_{17}H_{17}Br_2NO$	$C_{17}H_{17}I_2NO$
Formula weight	1289.95	411.138	505.14
Temperature/K	273.15	273.15	273.15
Crystal system	triclinic	monoclinic	monoclinic
Space group	*P*-1	$P2_1/c$	$P2_1/c$
a/Å	11.961(3)	12.0360(13)	12.2808(5)
b/Å	16.887(5)	16.8874(16)	17.2241(7)
c/Å	16.929(5)	17.194(2)	17.6053(6)
α/°	90	90	90
β/°	90	102.727(4)	102.992(1)
γ/°	103.800(8)	90	90
Volume/Å^3	3320.4(16)	3408.9(6)	3628.6(2)
Z	2	8	8
ρ_{calc}g/cm^3	1.29	1.602	1.849
μ/mm^{-1}	0.388	4.769	3.467
F(000)	1349	1629.6	1914.5
Crystal size/mm^3	0.112 × 0.112 × 0.112	0.111 × 0.111 × 0.111	0.349 × 0.23 × 0.084
Radiation	Mo Kα (λ = 0.71073)	Mo Kα (λ = 0.71073)	Mo Kα (λ = 0.71073)
2Θ range for data collection/°	2.4 to 50.5	3.42 to 52.84	4.38 to 54
Index ranges	$-15 \le h \le 15$, -19 $\le k \le 21$, -21 $\le l \le 21$	$-14 \le h \le 15$, -21 $\le k \le 21$, -21 $\le l \le 21$	$-16 \le h \le 16$, -23 $\le k \le 23$, -23 $\le l \le 22$
Reflections collected	46,796	52,193	62,659
Independent reflections	12,016 [R_{int} = 0.2526, R_{sigma} = 0.3810]	6984 [R_{int} = 0.1353, R_{sigma} = 0.0943]	7845 [R_{int} = 0.0915, R_{sigma} = 0.0569]
Data/restraints/parameters	12,016/0/773	6984/0/387	7845/0/387
Goodness-of-fit on F^2	0.884	0.996	1.015
Final R indexes [$I \ge 2\sigma$ (I)]	R_1 = 0.0825, wR_2 = 0.1650	R_1 = 0.0486, wR_2 = 0.0692	R_1 = 0.0482, wR_2 = 0.1217
Final R indexes [all data]	R_1 = 0.3350, wR_2 = 0.2833	R_1 = 0.1559, wR_2 = 0.0950	R_1 = 0.0739, wR_2 = 0.1430
Largest diff. peak/hole / e Å^{-3}	0.75/−0.82	0.95/−0.88	1.00/−1.64

5. Biological study

5.1. Stability study

Before assessing the biological potential of compounds, it is essential to confirm their chemical and structural stability under relevant conditions. Instability may lead to degradation, transformation, or precipitation, which can produce misleading biological data and reduce reproducibility. Stability studies ensure that the compounds retain their integrity during storage and experimental handling while also providing early insight into their suitability as therapeutic candidates. In this study, the stability of the synthesized compounds (SB1–SB3) was evaluated using time-dependent UV–vis spectroscopy, which revealed that all compounds maintained high stability under the experimental conditions.

Having established the chemical stability of the synthesized compounds (SB1–SB3), we evaluated their biological potential through cytotoxicity, antioxidant, and antibacterial assays to determine their therapeutic relevance.

5.2. Cytotoxicity study

The cytotoxicity of the synthesized compounds was evaluated against the ME180 cervical cancer cell line at concentrations of 1 μM and 2 μM, and the results were compared with methylglyoxal as a reference control. The activity of the compounds and the control drug against the tested cell lines is expressed in terms IC_{50} after 48 h of exposure. The results are presented in Table 2. The compound demonstrated better anticancer activity than the control, having IC_{50} values ranging from 0.60–1.03 μM (Table 2). Among the compounds, SB2, bromo-substituted, shows the lowest IC50 value (0.60 μM), followed by SB1, chloro-substituted, which has an IC50 value of 0.72 μM, while SB3, iodo-substituted, has an IC_{50}value of 1.03 μM. In contrast to the control, methylglyoxal has an IC_{50} value of 1.52 μM. In general, the trend of activity among the compounds is as follows: SB2>SB1>SB3.

The superior cytotoxicity of SB2 (dibromo-substituted) compared to SB1 (dichloro) and SB3 (diiodo) can be attributed to the balance of steric, electronic, and lipophilic effects imparted by the bromine atoms [47]. Bromine provides an optimal size and polarizability that enhances cell permeability and stabilises interactions such as halogen bonding and hydrophobic contacts with biomolecular targets [48]. In contrast, chlorine is smaller and less polarizable, offering weaker hydrophobic and electronic contributions, while iodine, though highly polarizable, is bulky and can distort molecular planarity, reduce the degree of solubility, and hinder effective binding. This explains why SB3 displayed the least activity, with the highest IC_{50}, as steric hindrance and solubility issues likely limited its bioavailability. Thus, the dibromo analogue (SB2) achieves the best balance, leading to the strongest biological response with the lowest IC_{50} value [49].

5.3. Antioxidant study

The antioxidant activity of the Schiff bases (SB1–SB3) was assessed using the DPPH radical scavenging method at 25 and 50 μM, with ascorbic acid serving as the reference standard (Table 3 and Fig. 2). All

Table 2
The IC_{50} values of the compounds and the control on the ME180 cell line.

Compounds	IC_{50} (μM)
SB1	0.74 ± 0.05
SB2	0.60 ± 0.30
SB3	1.03 ± 0.02
Methylglyoxal	1.52 ± 0.07
DMSO	–

Table 3
DPPH radical scavenging activity of the compound compared to the control.

Compounds	Scavenging rate (%)	
	25 μM	50 μM
SB1	37.60±0.43	38.80±0.42
SB2	34.70±0.76	36.80±0.35
SB3	36.90±0.44	37.30±0.42
Ascorbic acid	39.70±0.53	43.02±0.03

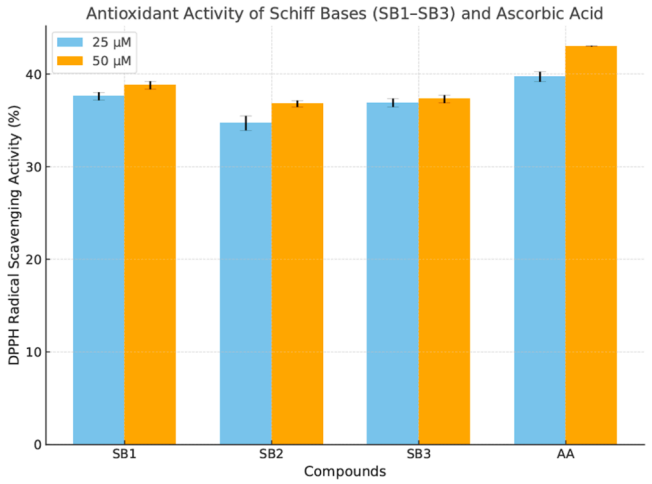

Fig. 2. Plot of the Radical Scavenging Activity of the compounds and the control at concentration of 25 and 50 μM; AA = Ascorbic acid.

compounds demonstrated a concentration-dependent increase in radical scavenging activity, indicating that higher concentrations enhanced the capacity to quench free radicals.

At the lower test concentration of 25 μM, SB1 (37.60 ± 0.43 %) and SB3 (36.90 ± 0.44 %) exhibited moderate scavenging activities that were statistically similar to each other ($p > 0.05$), but both were significantly higher than SB2 (34.70 ± 0.76 %, $p < 0.05$). The reference antioxidant, AA (39.70 ± 0.53 %), achieved the highest scavenging activity at this concentration and was significantly more potent than all Schiff base compounds ($p < 0.05$). Upon increasing the concentration to 50 μM, all compounds displayed an improvement in activity. SB1 (38.80 ± 0.42 %) remained the most active among the Schiff bases, followed by SB3 (37.30 ± 0.42 %) and SB2 (36.80 ± 0.35 %). Statistical analysis using one-way ANOVA followed by Tukey's post-hoc test revealed that AA (43.02 ± 0.03 %) retained a significantly higher antioxidant effect than SB1, SB2, and SB3 at this concentration ($p < 0.05$). Furthermore, SB1 demonstrated significantly greater activity than SB2 at both test concentrations ($p < 0.05$), whereas no significant difference was observed between SB3 and SB2 at 50 μM ($p > 0.05$). The order of activity across concentrations was therefore **SB1 > SB3 > SB2**, consistent with the notion that the electron-withdrawing effect of chlorine enhances phenoxyl radical stabilization more effectively than bromine or iodine [50,51]. These findings indicate that halogen substitution exerts a measurable influence on antioxidant efficiency, with chloro-substitution conferring the greatest benefit among the tested compounds

5.4. Antibacterial study

The antibacterial activities of the synthesized Schiff base compounds (SB1–SB3) were evaluated against two Gram-positive strains (*S. aureus* and *S. pyogenes*) and two Gram-negative strains (*E. coli* and *K. pneumoniae*) using the disc diffusion method at concentrations of 20 and 40 μM (Fig. 3, 4 and Table 4). Ciprofloxacin was used as the positive control, while DMSO served as the negative control.

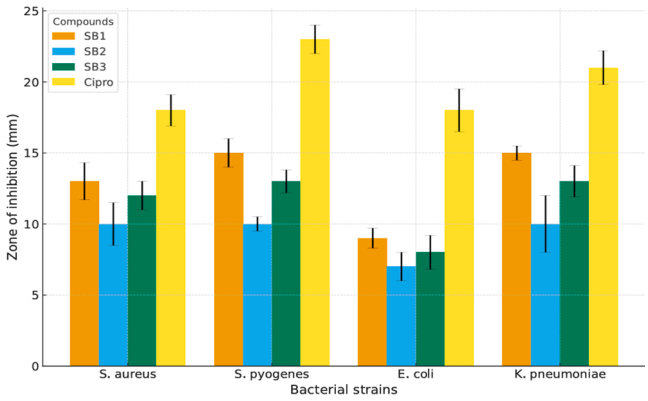

Fig. 3. Antibacterial activity of halogen-substituted Schiff base derivatives (**SB1–SB3**) and ciprofloxacin (Cipro) at **20 μM**, expressed as zones of inhibition (mm ± SD) against *S. aureus, S. pyogenes, E. coli*, and *K. pneumoniae*. SB1 exhibited the most pronounced inhibitory effect, particularly against *S. pyogenes* and *K. pneumoniae*, compared to other synthesized derivatives.

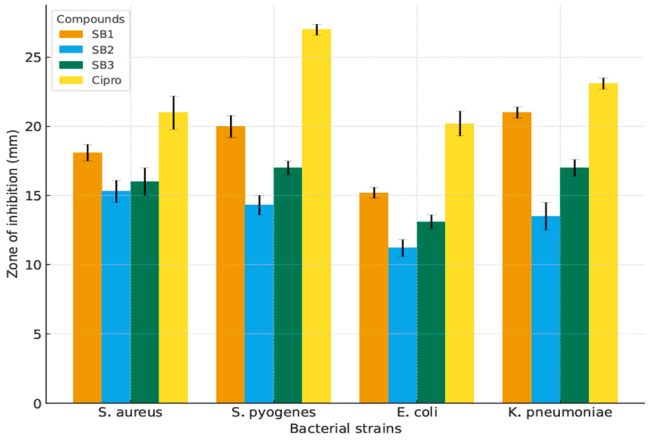

Fig. 4. Antibacterial activity of halogen-substituted Schiff base derivatives (**SB1–SB3**) and ciprofloxacin (Cipro) at **40 μM**, expressed as zones of inhibition (mm ± SD) against *S. aureus, S. pyogenes, E. coli*, and *K. pneumoniae*. The results reveal a clear concentration-dependent enhancement in activity, with SB1 maintaining the highest antibacterial potency across all tested strains.

Table 4
Minimum inhibitory concentration in (μg/mL) of the compounds and the control against the bacterial strains.

Compounds	S. aureus	S. pyogenes	*E. coli*	K. pneumonioe
SB1	15.62	15.62	31.25	15.62
SB2	62.50	62.50	NA	62.50
SB3	31.25	31.25	62.50	31.25
Ciprofloxacin	15.62	7.81	15.62	7.81

At 20 μM, all compounds exhibited moderate activity, with *S. pyogenes* and *K. pneumoniae* being the most sensitive organisms. SB1 consistently displayed higher inhibition zones (15 mm on *S. pyogenes* and *K. pneumoniae*) compared to SB2 and SB3, while SB2 was the least active across all strains (the lowest inhibition zone of 7 mm against *E. coli*).

At the higher concentration of 40 μM, the activities of the compounds improved in a dose-dependent manner. SB1 again showed superior performance, with inhibition zones of 21 mm (*K. pneumoniae*) and 20 mm (*S. pyogenes*), approaching those of ciprofloxacin. SB3 demonstrated intermediate potency, recording 17 mm against *S. pyogenes* and *K. pneumoniae*, while SB2 remained the least active with values ranging

from 11 to 15 mm.

Overall, the results establish the trend of activity as SB1 > SB3 > SB2, with Gram-positive bacteria being generally more susceptible than Gram-negative species. Furthermore, the minimum inhibitory concentration (MIC) results mirrored the trends observed in the zone of inhibition assays. It is evident that SB1 exhibited the lowest MIC value of 7.81 μg/mL against *S. pyogenes*, while displaying a higher MIC value of 31.25 μg/mL against *E. coli*. Conversely, SB2 showcased a minimal MIC value of 31.25 μg/mL against *S. pyogenes*, but a higher MIC value of 62.50 μg/mL against *S. aureus* and *K. pneumoniae*. SB3 displayed a lower MIC value of 15.62 μg/mL against *S. pyogenes*, with a higher MIC value of 31.25 μg/mL against *S. aureus* and *K. pneumoniae*. These findings align with the common observation that Gram-negative bacteria possess inherently more intricate and impermeable cell walls, rendering them less susceptible to a wide array of antimicrobial agents [52,53].

5.5. Relationship between lipophilicity(log P) and antibacterialactivity

The relationship between calculated lipophilicity (logP) and antibacterial activity is illustrated in Fig. 5. The compounds SB1–SB3 exhibit high lipophilicity (logP 5.65–5.97), typical of halogenated compounds. A moderate negative correlation ($r = -0.68$) was observed between logP and the mean zone of inhibition, indicating that higher lipophilicity corresponds to lower apparent antibacterial activity in the agar diffusion assay. This trend suggests that excessive hydrophobicity may limit aqueous solubility and diffusion through the agar medium, thereby reducing the effective concentration of the compound reaching the bacterial cells.

Among the series, SB1 (dichloro) showed the largest inhibition zones and an intermediate logP, while SB2 (dibromo) was the most lipophilic and exhibited the weakest antibacterial activity. SB3 (diiodo), with slightly lower logP than SB2, showed intermediate antibacterial efficacy. These findings support the notion that moderate lipophilicity favours antibacterial performance by balancing membrane permeability with sufficient aqueous solubility. Conversely, the higher logP of SB2 may contribute to its stronger cytotoxicity toward ME180 cancer cells, where enhanced cell membrane penetration is advantageous.

5.6. Influence of halogensubstitutionon biologicalactivity

The biological profiles of the synthesized Schiff base derivatives (SB1–SB3) reveal a clear dependence on the nature of halogen substituents on the salicylaldehyde ring. The compounds differ only in the type of halogen attached at the 3,5-positions, chlorine (SB1), bromine (SB2), and iodine (SB3), providing an excellent framework to explore how halogen size, electro negativity, and polarizability influence cytotoxic, antioxidant, and antibacterial activities

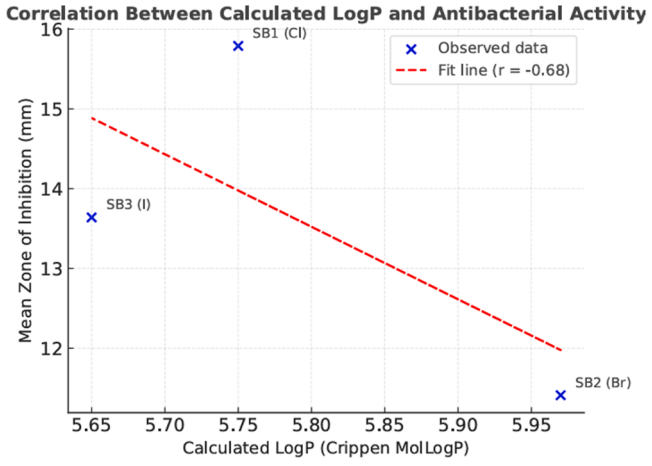

Fig. 5. Correlation between Calculated log P and Mean Antibacterial Activity of SB1–SB3.

5.7. Cytotoxic activity

As presented in Table 2, all compounds displayed pronounced cytotoxicity against the ME180 cervical cancer cell line, with IC_{50} values ranging from 0.60 to 1.03 μM, surpassing that of the reference methylglyoxal (1.52 μM). The bromo-substituted SB2 showed the highest potency ($IC_{50} = 0.60$ μM), followed by the chloro (SB1, 0.74 μM) and iodo (SB3, 1.03 μM) analogues.This trend (SB2 > SB1 > SB3) suggests that bromine substitution enhances lipophilicity and membrane permeability, facilitating stronger cellular uptake and interaction with intracellular targets, possibly via the azomethine linkage and phenolic groups. The moderate atomic size and polarizability of bromine may also enable optimal π–π or hydrophobic interactions with biomolecular sites, thereby promoting cytotoxic efficacy [54].

5.8. Antioxidant activity

The DPPH radical scavenging data (Table 3) revealed a contrasting trend (SB1 > SB3 > SB2). The chloro-substituted compound exhibited the highest scavenging ability, approaching the activity of ascorbic acid. This enhancement can be attributed to chlorine's strong electron-withdrawing ability, which stabilizes the phenoxy radical formed during hydrogen atom transfer. In contrast, the weaker electronegativity and larger atomic radius of bromine in SB2 reduce the efficiency of radical stabilization, leading to lower antioxidant potential. Iodine, while highly polarizable, introduces steric hindrance that partially offsets its ability to delocalize unpaired electrons.

Thus, the antioxidant data emphasize that electron-withdrawing strength and minimal steric interference favour radical scavenging efficiency—parameters best satisfied by the chlorine substituent [55].

5.9. Antibacterial activity

The antibacterial evaluation (MIC), Table 4, against two Gram-positive (*S. aureus* and *S. pyogenes*) and two Gram-negative (*E. coli*and *K. pneumoniae*) strains further supports the antioxidant trend. The chloro-derivative SB1 exhibited the most potent and broad-spectrum antibacterial effect, with minimum inhibitory concentrations (MICs) as low as 15.62 μg/mL against both Gram-positive and Gram-negative bacteria. The iodo-substituted SB3 displayed moderate inhibition (31.25–62.50 μg/mL), while the bromo analogue SB2 showed the weakest activity and was inactive against *E. coli*.

This pattern indicates that antibacterial activity correlates with electron-withdrawing capability and molecular compactness, both of which favour enhanced binding to bacterial enzymes or cell wall components. The smaller and more electronegative chlorine atom in SB1 likely increases the overall polarity and dipole moment of the molecule, improving its interaction with bacterial membranes. Conversely, the bulky bromine substituent in SB2 may hinder diffusion through bacterial cell walls, explaining its poor antibacterial response despite high cytotoxic potency.

5.10. Comparative structure–activityrelationship(SAR)

The biological activities of the synthesized Schiff bases (SB1–SB3) are strongly influenced by the nature of the halogen substituents, as summarized in Table 5. The table presents key electronic and steric properties, electro negativity and atomic radius, alongside the observed trends in cytotoxicity, antioxidant activity, and antibacterial potency.

Taken together, the biological results underscore the nuanced role of halogen substitution in modulating bioactivity. The inverse relationship between cytotoxicity and both antioxidant/antibacterial activities (Fig. 6), suggests that different mechanisms dominate these bio-effects.

Table 5
Influence of halogen substitution on the biological activities of Schiff bases (SB1–SB3) and associated electronic/steric properties. Electro negativity and atomic radius of the halogen substituents are shown alongside trends in cytotoxicity, antioxidant, and antibacterial activities.

Compound	Substituent	Electro negativity (Pauling)	Atomic Radius (pm)	Cytotoxicity	Antioxidant	Antibacterial
SB1	Cl	3.16	99	Moderate	Highest	Highest
SB2	Br	2.96	114	Highest	Lowest	Lowest
SB3	I	2.66	133	Lowest	Moderate	Moderate

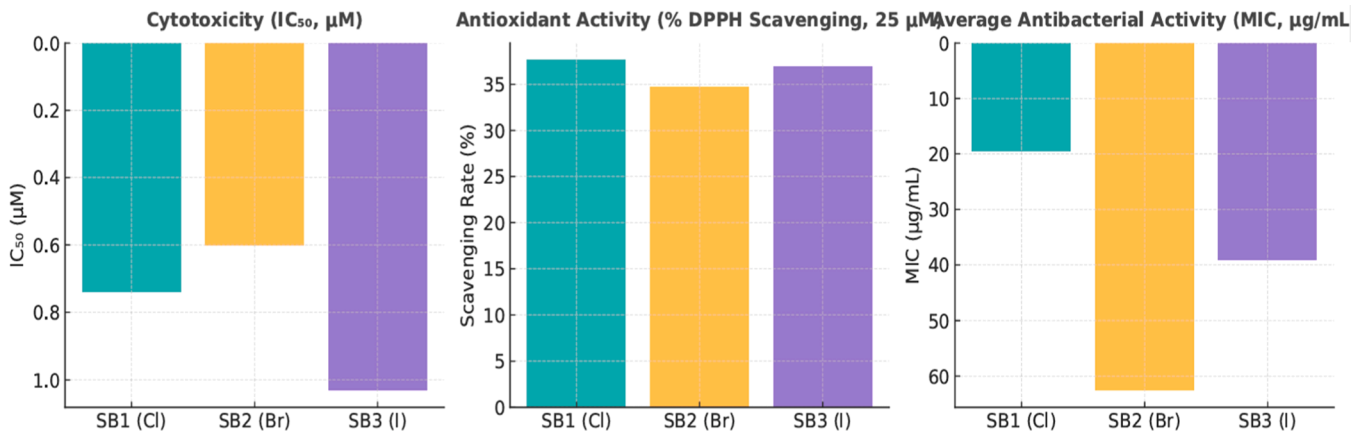

Fig. 6. Comparative biological activities of halogen-substituted Schiff bases (SB1–SB3). The figure illustrates the influence of halogen substitution (Cl, Br, I) on (a) cytotoxicity (IC_{50} values against ME180 cervical cancer cell line), (b) antioxidant activity (DPPH radical scavenging at 25 μM), and (c) antibacterial activity (average MIC values against *S. aureus, S. pyogenes, E. coli*, and *K. pneumoniae*). Lower IC_{50} and MIC values indicate stronger activity.

Cytotoxicity appears to depend on lipophilicity and cellular uptake, while antioxidant and antibacterial properties are governed by electronic effects and hydrogen-donating capacity. SB2's strong cytotoxicity but poor antioxidant and antibacterial activity therefore reflect its higher lipophilicity but weaker electron-withdrawing behaviour, resulting in improved membrane penetration in mammalian cells but diminished redox and antibacterial efficiency.

5.11. Molecular docking study

To ensure the reliability of the docking procedure, pose validation was performed by redocking the co-crystallized ligand into the MMP-9 active site. The reproduced pose showed a strong overlap with the experimental orientation (RMSD = 0.161 Å; Supplementary Figure S20), confirming the accuracy of the docking protocol. The molecular docking results and key interactions of the synthesized compounds (SB1-SB3) and methylglyoxal within the active site of metalloprotease are provided in Fig. 7. The compounds, SB1, SB2, and SB3 showed favourable binding energies (−6.27, −5.74, and −6.16 kcal/mol, respectively), while the control (methylglyoxal) had a markedly lower binding energy (−2.35 kcal/mol). All compounds formed hydrogen bonds with Glu402 and coordinated with the catalytic Zn^{2+} ion *via* the phenolate oxygen and carbonyl moieties in the control. This indicates that the interaction is crucial for anchoring ligands at the active site. Structural differences, especially in halogen substitution, significantly influenced binding affinity. SB1-SB3 shared a conserved aromatic ring that enabled π–π stacking interactions with His411, enhancing stability. The variation in halogen atoms (Cl, Br, I) affected the strength and geometry of halogen bonding. As shown in Fig. 7A, SB1, with smaller chlorine atoms, formed more directional halogen bonds, likely contributing to its slightly higher docking score. Conversely, SB2 and SB3, with bulkier Br and I atoms (Figs. 7B and C), exhibited slightly weaker affinities, possibly due to steric hindrance, despite forming similar halogen bonds. Methylglyoxal lacks the halogenated aryl moiety present in SB1-SB3, resulting in the absence of both π–π stacking and halogen bonds (Fig. 7D). This structural deficiency correlates with its weaker binding energy affinity, underscoring the critical role of aromaticity and halogenation in protein-ligand stabilization. Hydrophobic interactions with residues such as Phe110, Leu187, Leu188, Ala189, Ala191, Val398, Tyr420, Pro421, Met422, and Tyr423, further stabilized SB1-SB3, but were minimal in methylglyoxal. Overall, the combined presence of metal-coordinating groups, halogenated aromatic systems, and π–π stacking capacity accounted for the stronger binding interactions of SB1-SB3. These structural features are therefore vital for enhancing affinity and specificity toward the metalloprotease active site. These results corroborated well with the data obtained from the biological study, showcasing SB1 and SB3 as the most biologically active in both assays.

5.12. Molecular dynamics simulations

Fig. 8 presents MDS analyses of SB1-SB3 and methylglyoxal complexes over 150 ns, evaluating their structural stability and dynamic behaviour using RMSD, RMSF, and SASA metrics, in comparison with the unbound protein (1GKC). The RMSD plot (Fig. 8A) revealed that all ligand-bound complexes exhibited lower fluctuations than the unbound protein, indicating improved structural stability upon ligand binding. Among them, SB1 and SB3 maintained the lowest RMSD values (~1.5–2.0 Å), suggesting high structural rigidity and stable binding throughout the simulation. SB2 and methylglyoxal showed moderate fluctuations, while the unbound protein displayed the highest structural deviation pattern (~2.5–3.2 Å).RMSF analysis (Fig. 8B) further confirmed these findings, showing that residue-level fluctuations were minimized in SB1 and SB3 complexes, particularly around the active site (residues 180–220). SB2 exhibited slightly higher fluctuations near residue 230, indicating localized flexibility that may affect binding stability. The unbound protein displayed higher overall residue mobility, particularly at the loop regions, reinforcing the stabilizing effect of ligand binding. The SASA results (Fig. 8C) established the differences in solvent accessibility. SB1 and SB3 demonstrated consistently lower SASA values, indicating compact conformations with minimal solvent exposure. SB2 exhibited increased SASA (~200–250 $Å^2$), likely due to partial exposure of hydrophobic regions, which may contribute to

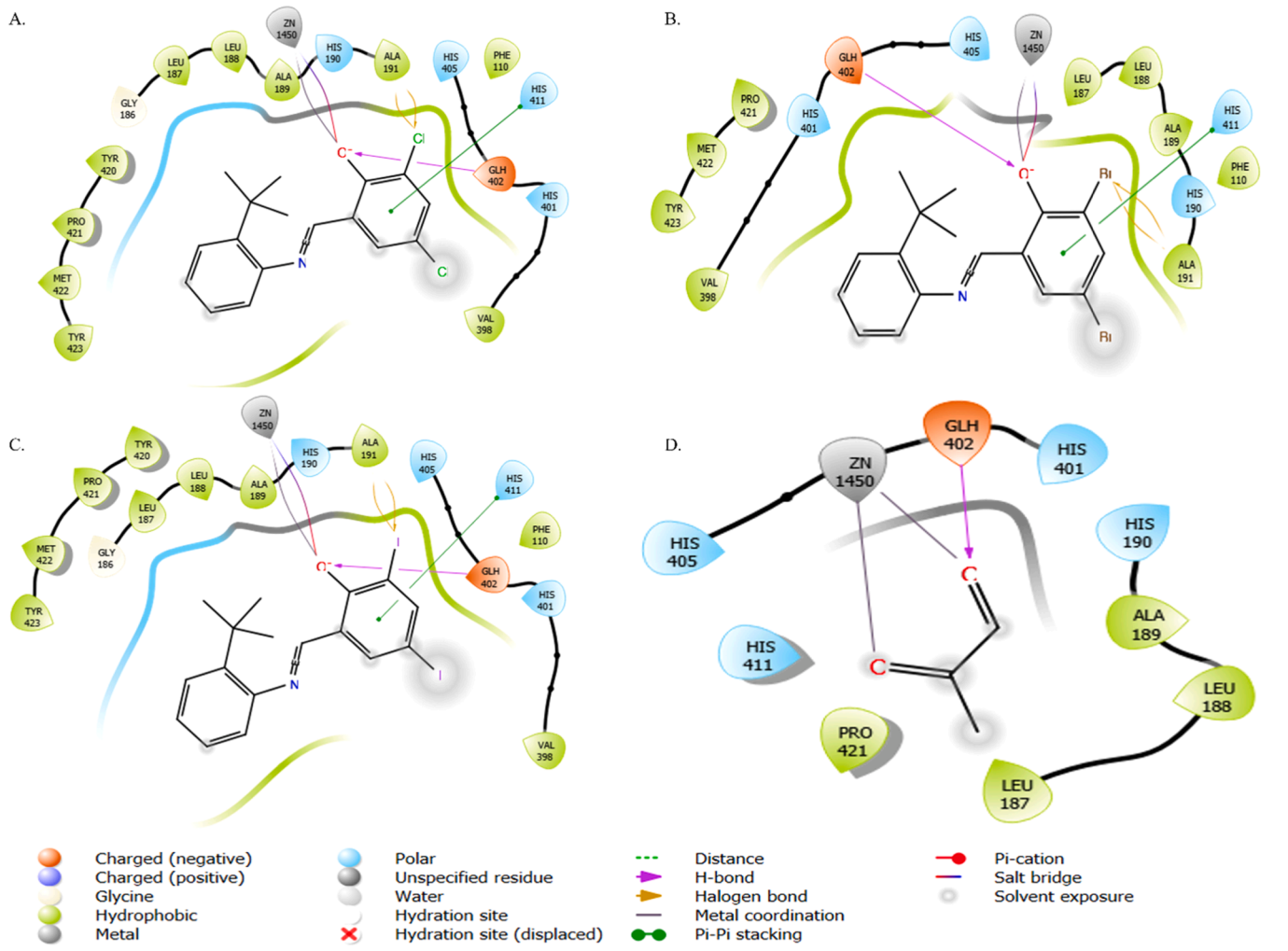

Fig. 7. Two-dimensional structure of the synthesized compounds, and methylglyoxal within the active site of 1GKC. Figs. 6A, 6B, 6C, and 6D present the binding interactions of **SB1, SB2, SB3**, and methylglyoxal, respectively.

its reduced binding affinity. Methylglyoxal showed fluctuating SASA values, indicating unstable interactions and poor burial within the binding pocket. These MD findings corroborate the docking results, highlighting SB1 and SB3 as the most stable and tightly bound inhibitors of 1GKC in this study. Their favourable RMSD, low RMSF, and SASA profiles support their potential as robust metalloprotease inhibitors. Figure S21 further supports these findings by depicting the interaction lifetimes of SB1–SB3 and methylglyoxal within the active site of the protein. Interestingly, the complex formed by SB1–SB3 consistently maintained strong and long-lasting interactions, dominated by ionic bonds involving His401, Glu402, His405, andHis411. These interactions were sustained for most of the trajectories, reflecting their high binding persistence. In contrast, hydrophobic contacts were more transient, contributing to minor fluctuations around the binding pocket. Methylglyoxal, however, exhibited weak and short-lived contacts distributed across several residues, and with no consistent ionic interactions. This signifies poor binding affinity and unstable complex formation. Collectively, dynamic behaviour and interaction analyses reinforce that SB1 and SB3 are the most stable and tightly bound inhibitors of 1GKC, exhibiting superior structural stability and stronger active-site engagement compared to SB2 and methylglyoxal.

5.13. Structural overview, physicochemical, and drug-likeness properties of the compounds

The synthesized compounds, SB1-SB3, differ only in the halogen substituents at the ortho and para positions of the salicyl ring: chlorine (SB1), bromine (SB2), and iodine (SB3). The substitution pattern directly influenced molecular weight (MW), molar refractivity (MR), and polarizability. As expected, MW and MR increased with the atomic size of the halogen: SB1 (Cl, MW = 322.23) < SB2 (Br, MW = 411.13)< SB3 (I, MW = 505.13) (Table 6). This trend also translated into increasing molecular polarizability, which might influence a higher lipophilicity and decreased aqueous solubility. All the compounds also had 3 rotatable bonds, 2 H-bond acceptors, and 1 donor (Table 6), indicating similar molecular flexibility and potential for passive membrane diffusion. SB1-SB3 maintained a consistent total polar surface area (~32.59 Å^2), supporting good permeability

However, their halogen-driven increases in MW (322.23 to 505.13) and logP (5.65 to 5.97) led to progressively more drug-likeness violations. SB3, with the largest halogen atoms (iodine), incurred two Lipinski violations [57,58], while SB1 had the least. In addition, LogS, Ali, and Silicos-IT models all classified the compounds as poorly soluble, with decreasing solubility from SB1 to SB3. Methylglyoxal, structurally distinct with its two carbonyl groups and lack of aromaticity, was highly hydrophilic (consensus logP = −0.24) and highly soluble in all models, supporting its classification as “highly soluble.” All compounds had moderate synthetic accessibility (2.75–3.10), yet Brenk alerts and lead-likeness violations highlight the presence of potentially reactive or non-ideal groups. Methylglyoxal obeys Lipinski’s rules due to its minimal molecular framework.

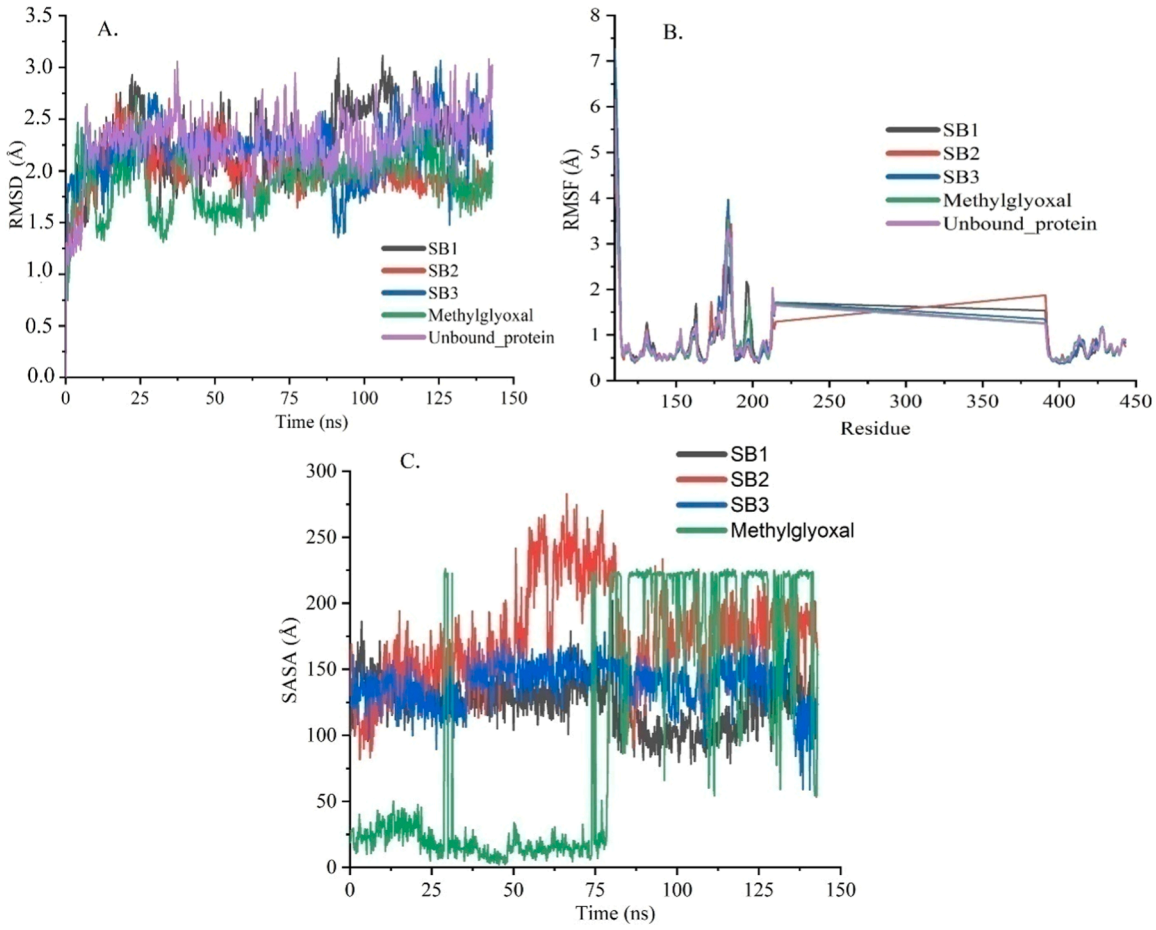

Fig. 8. MD simulation trajectory analysis of the unbound protein (1GKC), Schiff base compounds (**SB1**-**SB3**), and methylglyoxal at the active site of 1GKC during a simulation run at 150 ns. The Figure presents a plot of (A) the RMSD calculated, (B) the RMSF, and (C) the SASA for the backbone protein.

Table 6
Physicochemical and drug-likeness profiling of **SB1**-**SB3**, and methylglyoxal. HBAs: Hydrogen bond acceptors, HBDs: Hydrogen bond donors, TPSA: Topological Polar Surface Area, Log S: logarithm (base 10) of the compound's solubility in water, SA: Synthetic accessibility.

Compounds	Formula	MW	RTBs	HBAs	HBDs	MR	TPSA	Log P	Log S	Ali Class	SA
SB1	$C_{17}H_{17}Cl_2NO$	322.23	3	2	1	91.45	32.59	5.75	−5.71	Poorly soluble	2.75
SB2	$C_{17}H_{17}Br_2NO$	411.13	3	2	1	96.83	32.59	5.97	−6.34	Poorly soluble	2.83
SB3	$C_{17}H_{17}I_2NO$	505.13	3	2	1	106.86	32.59	5.65	−6.88	Poorly soluble	3.10
Methylglyoxal	$C_3H_4O_2$	72.06	1	2	0	16.93	34.14	−0.24	0.02	Highly soluble	1.00

5.14. Pharmacokinetics

All the compounds showed high gastrointestinal (GI) absorption, likely attributed to their small TPSA and balanced lipophilicity. SB1 and SB3 were predicted to cross the blood-brain barrier (BBB), whereas SB2 and methylglyoxal were BBB non-permeable (Table 7). None of the compounds were substrates for P-glycoprotein (Pgp), reducing concerns of efflux-mediated resistance. However, they all of them inhibited multiple cytochrome P450 enzymes (CYP1A2, 2C19, 2C9) (Table 7), potentially due to the planar aromatic systems and halogen substituents, which are known to modulate CYP binding [56]. SB3 uniquely did not inhibit CYP2D6 or CYP3A4, possibly due to steric hindrance from iodine atoms. Methylglyoxal showed no CYP inhibition, aligning with its small size and lack of complex functional groups.

Table 7
Pharmacokinetics and toxicological profile of the compounds.

Parameters	SB1	SB2	SB3	Methylglyoxal
GI absorption	High	High	High	High
BBB permeant	Yes	No	Yes	No
Pgp substrate	No	No	No	No
CYP1A2 inhibitor	Yes	Yes	Yes	No
CYP2C19 inhibitor	Yes	Yes	Yes	No
CYP2C9 inhibitor	Yes	Yes	Yes	No
CYP2D6 inhibitor	Yes	Yes	No	No
CYP3A4 inhibitor	No	No	No	No
Lipinski violations	1	1	2	0
Hepatocytotoxicity	No	No	No	No
Ames	No	No	No	Yes
Total clearance	0.21	−0.02	−0.45	0.68

5.15. Toxicity and clearance

None of the compounds were flagged for hepatotoxicity or Ames mutagenicity, supporting their relative safety. In contrast, methylglyoxal tested positive in Ames prediction, consistent with its electrophilic aldehyde groups known to form DNA adducts and cause mutagenicity [56]. Predicted total clearance values were very low for

the SB series, with negative clearance estimates, suggesting longer systemic retention. Methylglyoxal had the highest clearance, likely due to rapid metabolic turnover. Log Kp values indicated reasonable skin permeability for SB1–SB3, with decreasing permeability as size and halogen weight increased. Methylglyoxal exhibited low skin permeability, consistent with its high polarity.

6. Conclusion

In this study, three halogen-substituted Schiff base ligands (SB1–SB3) were successfully synthesized through the condensation of 2-tert-butylaniline with 3,5-dichloro-, 3,5-dibromo-, and 3,5-diiodosalicylaldehyde, respectively, and their structures were validated using ^{1}H and ^{13}C NMR, SCXRD, FTIR, UV–Vis, mass spectrometry, and elemental analysis (CHN). The spectroscopic and analytical data confirmed the formation and purity of the target compounds. Biological evaluations demonstrated that the compounds possessed promising cytotoxic, antioxidant, and antibacterial activities. Among them, SB1 (chloro-substituted) consistently exhibited the strongest activity across all assays, followed by SB3 (iodo-substituted), while SB2 (bromo-substituted) showed comparatively weaker responses. These findings highlight the significant influence of halogen substitution on the biological performance of Schiff bases and underscore the importance of structure–activity relationship (SAR) analysis in guiding the design of bioactive molecules. Complementary computational studies further corroborated well with the data obtained from the biological study, showcasing SB1 and SB3 as the most promising compounds. Physicochemical profiling also revealed that increasing halogen size enhanced molecular weight and lipophilicity, thereby influencing solubility and drug-likeness. Importantly, all compounds demonstrated high gastrointestinal absorption and relative safety, although multiple CYP enzyme inhibitions were predicted. This highlights the propensity of the compounds and the need for their further optimization as potential multifunctional agents.

CRediT authorship contribution statement

Tsholofelo S. Nthehang: Writing – review & editing, Writing – original draft, Project administration, Methodology, Formal analysis, Data curation. **Ibrahim Waziri:** Writing – review & editing, Writing – original draft, Visualization, Validation, Supervision, Software, Resources, Project administration, Methodology, Investigation, Funding acquisition, Formal analysis, Data curation, Conceptualization. **Tunde L. Yusuf:** Writing – review & editing, Writing – original draft, Visualization, Validation, Software, Formal analysis, Data curation. **Samson O. Oselusi:** Writing – review & editing, Writing – original draft, Visualization, Validation, Software, Methodology, Investigation, Formal analysis, Data curation. **Alfred J. Muller:** Writing – original draft, Visualization, Validation, Supervision, Software, Resources, Project administration, Methodology, Investigation, Funding acquisition, Formal analysis, Data curation, Conceptualization.

Declaration of competing interest

The authors declare no conflict of interest.

Acknowledgements

Dr. Ibrahim Waziri expresses gratitude to the University Research Center (URC) for the Postdoctoral research fellowship award. Tsholofelo S. Nthehang extends thanks to the South African National Research Foundation (NRF) for the M.*Sc.* bursary and to the National Research Foundation (NRF) (Grant No: 111706) for covering running expenses.

Supplementary materials

Supplementary material associated with this article can be found, in the online version, at doi:10.1016/j.molstruc.2025.144508.

Supplementary materials: The crystallographic data for compounds **SB1** (CCDC 2483727), **SB2** (CCDC 2483725), and **SB3** (CCDC 2483726) are available as supplementary information. These data can be accessed free of charge from the Cambridge Crystallographic Data Centre via http://www.ccdc.cam.ac.uk/data_request/cif. Additional supporting information related to this article can be found in the online version at the Supplementary material associated with this article.

Data availability

Data will be made available on request.

References

[1] S. Reza, R. Anjum, R.Z. Khandoker, S.R. Khan, M.R. Islam, S.M.R. Dewan, Gynecol. Oncol. Rep. 54 (2024) 101460.
[2] O. Omotoso, J.O. Teibo, F.A. Atiba, T. Oladimeji, O.K. Paimo, F.S. Ataya, G.E.-S. Batiha, A. Alexiou, Int. J. Equity. Health 22 (2023) 189.
[3] X. An, W. Yu, J. Liu, D. Tang, L. Yang, X. Chen, Cell Death. Dis. 15 (2024) 556.
[4] D. Tan, N. Ma, Y. Wang, X. Li, M. Xu, Cell Stress and Chaperones (2025) 100108.
[5] M.J. Iqbal, A. Kabeer, Z. Abbas, H.A. Siddiqui, D. Calina, J. Sharifi-Rad, W.C. Cho, Cell Commun. Signal. 22 (2024) 7.
[6] M.A. Salam, M.Y. Al-Amin, M.T. Salam, J.S. Pawar, N. Akhter, A.A. Rabaan, M. A. Alqumber, Antimicrobial resistance: a Growing Serious Threat for Global Public Health, Healthcare. MDPI, 2023, p. 1946.
[7] M. Daud, B. Nyombi, South Asian J. Res. Microbiology 6 (2020) 33–39.
[8] M.M. Aljeldah, Antibiotics 11 (2022) 1082.
[9] K.W.K. Tang, B.C. Millar, J.E. Moore, Br. J. Biomed. Sci. 80 (2023) 11387.
[10] M. Ferri, E. Ranucci, P. Romagnoli, V. Giaccone, Crit. Rev. Food Sci. Nutr. 57 (2017) 2857.
[11] M.A.A. Majumder, S. Rahman, D. Cohall, A. Bharatha, K. Singh, M. Haque, M. Gittens-St Hilaire, Infect. Drug Resist. (2020) 4713.
[12] M. Aijaz, M. Ahmad, M.A. Ansari, S. Ahmad, Int. J. Pharm. Drug Des 1 (2023) 7.
[13] A. Shafie, A.A. Ashour, J. Inorg. Biochem. (2025) 112909.
[14] R. Malav, S. Ray, RSC. Adv. 15 (2025) 22889.
[15] R.N. Yadav, M.F. Hossain, D. Ray, A. Kumar Srivastava, B.K. Banik, Catal. Rev. 67 (2025) 579.
[16] N. Kordestani, H.A. Rudbari, A.R. Fernandes, L.R. Raposo, A. Luz, P.V. Baptista, G. Bruno, R. Scopelliti, Z. Fateminia, N. Micale, Dalton Trans. 50 (2021) 3990.
[17] Y.W. Dong, R.Q. Fan, X.M. Wang, P. Wang, H.J. Zhang, L.G. Wei, Y. Song, X. Du, W. Chen, Y.L. Yang, Eur. J. Inorg. Chem. 2016 (2016) 3598.
[18] I. Waziri, T.L. Yusuf, H.A. Zarma, S.O. Oselusi, L.-C.C. Coetzee, A.S. Adeyinka, Inorganica Chimica Acta 552 (2023) 121505.
[19] L. Jiao, M. Huang, J. Xu, Q. Yang, Q. Wu, J. Mol. Struct. 1312 (2024) 138676.
[20] M. Coandă, C. Limban, D.C. Nuță, Antibiotics 13 (2024) 75.
[21] S. Bargujar, S. Ratnani, R. Jain, Inorg. Chem. Commun. 162 (2024) 112250.
[22] G.M. Sheldrick, Foundat. Crystallogr. 46 (1990) 467.
[23] T. Schulz, K. Meindl, D. Leusser, D. Stern, J. Graf, C. Michaelsen, M. Ruf, G. M. Sheldrick, D. Stalke, Applied Crystallography 42 (2009) 885.
[24] G.M. Sheldrick, Crystal Structure Communications 71 (2015) 3.
[25] C.F. Macrae, I. Sovago, S.J. Cottrell, P.T. Galek, P. McCabe, E. Pidcock, M. Platings, G.P. Shields, J.S. Stevens, M. Towler, Appl. Crystallogr. 53 (2020) 226.
[26] C.F. Macrae, I.J. Bruno, J.A. Chisholm, P.R. Edgington, P. McCabe, E. Pidcock, L. Rodriguez-Monge, R. Taylor, J. Streek, P.A. Wood, Appl. Crystallogr. 41 (2008) 466.
[27] M. Domińska, G. Pastuch-Gawołek, A. Domiński, P. Kurcok, K. Erfurt, Molecules. 27 (2022) 1040.
[28] İ. Gulcin, S.H. Alwasel, Processes 11 (2023) 2248.
[29] M. Zaidan, A. Noor Rain, A. Badrul, A. Adlin, A. Norazah, I. Zakiah, Trop. Biomed. 22 (2005) 165.
[30] S. Rowsell, P. Hawtin, C.A. Minshull, H. Jepson, S.M. Brockbank, D.G. Barratt, A. M. Slater, W.L. McPheat, D. Waterson, A.M. Henney, J. Mol. Biol. 319 (2002) 173.
[31] W. Chen, S. Huang, K. Shi, L. Yi, Y. Liu, W. Liu, Cancer Control 28 (2021) 10732748211033743.
[32] I. Vanlaere, C. Libert, Clin. Microbiol. Rev. 22 (2009) 224.
[33] C. Lu, C. Wu, D. Ghoreishi, W. Chen, L. Wang, W. Damm, G.A. Ross, M.K. Dahlgren, E. Russell, C.D. Von Bargen, J. Chem. Theory. Comput. 17 (2021) 4291.
[34] S.O. Oselusi, S.A. Egieyeh, A. Christoffels, Molecules. 26 (2021) 3674.
[35] S. Vijayraghavan, N. Saini, Chem. Res. Toxicol. 36 (2023) 983.
[36] E.V. Panova, D.A. Safin, J. Mol. Struct. 1323 (2025) 140443.
[37] M. Bouhdada, M.E. Amane, H.E. Hamdani, Z. Khiya, J. Mol. Struct. 1271 (2023) 134026.
[38] S. Van Vliet, J. Sheng, C.N. Stindt, B.L. Feringa, Nat. Commun. 15 (2024) 6461.
[39] A. Xing, D. Zeng, Z. Chen, J. Mol. Struct. 1253 (2022) 132209.
[40] M. Shanmugam, K. Narayanan, K.H. Prasad, D. Karthikeyan, L. Chandrasekaran, R. Atchudan, V. Chidambaranathan, New J. Chem. 42 (2018) 1698.
[41] N.P. Ebosie, M.O. Ogwuegbu, G.O. Onyedika, F.C. Onwumere, J. Iranian Chem. Society 18 (2021) 3145.
[42] R. Nagar, J. Inorg. Biochem. 40 (1990) 349.
[43] M. Pocheć, K.M. Krupka, J.J. Panek, K. Orzechowski, A. Jezierska, Molecules. 27 (2022) 1225.

[44] T. De Toledo, P. Pizani, L. Da Silva, A. Teixeira, P. Freire, J. Mol. Struct. 1097 (2015) 106.
[45] E. Tas, I. Ucar, V.T. Kasumov, A. Kilic, A. Bulut, Spectrochimica Acta Part A: Molec. Biomolec. Spectros. 68 (2007) 463.
[46] N.H. Nasaruddin, S.N. Ahmad, S.S. Sirat, K.W. Tan, N.A. Zakaria, S.S. Mohamad Nazam, N.M.M.A. Rahman, N.S. Mohd Yusof, H. Bahron, ACS. Omega 7 (2022) 42809.
[47] R.M. Ramadan, H.H. El-Shalakany, M.A. Sayed, Sci. Rep. 15 (2025) 18546.
[48] E. Potapskyi, K. Kustrzyńska, D. Łażewski, P. Skupin-Mrugalska, R. Lesyk, M. Wierzchowski, J. Med. Sci. 93 (2024) e1128.
[49] R.M. Elsamra, M.S. Masoud, A.M. Ramadan, Sci. Rep. 12 (2022) 20192.
[50] K. Rajimon, N. Elangovan, A.A. Khairbek, R. Thomas, J. Mol. Liq. 370 (2023) 121055.
[51] G.A. Mala, H.B. Friedrich, H. Ibrahim, N.P. Ndahi, S.J. Zamisa, D.S. Masokano, I. Waziri, M. Singh, Bioorg. Chem. (2025) 108638.
[52] N. Kordestani, H.A. Rudbari, A.R. Fernandes, L.R. Raposo, A. Luz, P.V. Baptista, G. Bruno, R. Scopelliti, Z. Fateminia, N. Micale, Dalton Transactions 50 (2021) 3990.
[53] S. Prasad, V. Radhakrishna, T.K. Ravi, Arab. J. Chem. 12 (2019) 3943.
[54] I. Waziri, T.L. Yusuf, E. Akintemi, M.T. Kelani, A. Muller, J. Mol. Struct. 1273 (2023) 134382.
[55] T.L. Yusuf, I. Waziri, S.D. Oladipo, M.S. Abd El-Maksoud, A.J. Muller, B. Vatsha, A. C.S. omega (2025).
[56] T.K. Karami, S. Hailu, S. Feng, R. Graham, H.J. Gukasyan, J. Ocular Pharmacol. Therapeut. 38 (2022) 43.
[57] S. Kralj, M. Jukič, U. Bren, Encyclopedia (Basel,. 2021) 3 (2023) 501.
[58] J. Ma, H. Yu, G. Li, T. An, J. Hazard. Mater. 473 (2024) 134589.